Kaykan, L. S. (2024). Magnetite-based hybrid cathode material for advanced lithium-ion batteries. *Actual Issues of Modern Science. European Scientific e-Journal, 34*, __-__. Ostrava: Tuculart Edition, European Institute for Innovation Development.

DOI: 10.47451/inn2024-11-01

The paper is published in Crossref, ICI Copernicus, BASE, Zenodo, OpenAIRE, LORY, Academic Resource Index ResearchBib, J-Gate, ISI International Scientific Indexing, ADL, JournalsPedia, Scilit, EBSCO, Mendeley, and WebArchive databases.

Larysa S. Kaykan, Doctor of Physical and Mathematical Sciences, Senior Researcher, Laboratory for Physics of Magnetic Films No. 23, G. V. Kurdyumov Institute for Metal Physics of the National Academy of Sciences of Ukraine. Kyiv, Ukraine.
ORCID: 0000-0002-4885-510X, Scopus: 57210702434

Magnetite-based hybrid cathode material for advanced lithium-ion batteries

Abstract: This research focuses on the synthesis, structural characterization, and electrochemical performance of a hybrid cathode material based on nano-dispersed magnetite for advanced lithium-ion batteries. The material was synthesized using a hydrothermal method that enabled the integration of magnetite into a mesoscopic framework, resulting in a hybrid structure optimized for electrochemical applications. Structural analysis using X-ray diffraction confirmed the X-ray amorphous nature of the compound, indicating a highly disordered atomic arrangement. Mössbauer spectroscopy further revealed the absence of a magnetically ordered state of iron, with paramagnetic doublets indicating Fe^{3+} cations in a symmetric oxygen coordination environment. These findings highlight the structural uniqueness of the material, with its nanoscale dispersion and amorphous properties playing a critical role in its electrochemical behavior. The electrochemical characterization demonstrated a stable discharge curve with an operating voltage of approximately 2.2 V, making it well-suited for low-voltage energy storage systems. The material exhibited a specific electrochemical capacity of ~350 A·h/kg, consistently maintained over three discharge cycles, reflecting its robust cycling stability and excellent structural durability. Potentiodynamic measurements and electrochemical impedance spectroscopy were used to calculate the lithium-ion diffusion coefficient, which ranged from ($3.0\ 10^{-13}$) to ($8.9\ 10^{-13}$) cm^2/s. These high diffusion values suggest efficient ionic transport facilitated by the amorphous structure and nanoscale distribution of magnetite within the composite. The hybrid material's structural features, such as its mesoscopic organization and enhanced lithium intercalation pathways, provide a strong basis for its performance. As indicated by the flat discharge profile, the absence of significant polarization effects during cycling demonstrates the material's capability for efficient charge transfer and reduced resistance at the electrode-electrolyte interface. The high stability of the lithium intercalation process, supported by the disordered yet stable structure, ensures consistent energy delivery over multiple cycles.

Keywords: lithium-ion batteries, nanomaterials, hybrid composites, electrochemical studies, XRD studies, Mössbauer studies, energy storage.

Introduction

The continuous advancements in portable electronics, electric vehicles, and renewable energy systems have necessitated the development of energy storage devices with higher capacity (*Heydari Gharahcheshmeh & Chowdhury, 2024*; *Mendonça et al., 2025*; *Su et al., 2024*), longer lifespans,

and improved safety. Lithium-ion batteries (LIBs) remain at the forefront of these efforts due to their superior energy density, efficiency, and rechargeability compared to other energy storage technologies (*Yang et al., 2024*; *Hou et al., 2025*). Central to the performance of LIBs is the development of novel electrode materials that can accommodate rapid ion diffusion, sustain high charge-discharge rates, and exhibit stability over extended cycling.

Nano-dispersed magnetite (Fe_3O_4) has garnered substantial interest in this context (*Li et al., 2024*) owing to its unique physicochemical properties and the broad spectrum of potential applications. Magnetite's versatility lies in its ability to be synthesized in various morphologies and sizes, tailored to specific requirements by adjusting production methods and conditions. For instance, as highlighted in (*Jonak & Borah, 2021*; *Adi & Taniguchi, 2022*), the combination of mechanochemical synthesis and ultrasonic dispersion can yield hollow spherical magnetite nanoparticles with an average size of 6-12 nm. These features make magnetite attractive for energy storage and open avenues for its use in diverse fields such as biology and medicine, where specific nanoparticle geometries play a critical role.

In LIB applications, magnetite demonstrates promising electrochemical properties as an electrode material. Its high theoretical capacity (924 mAh g^{-1}) (*Zeng et al., 2025*) surpasses many conventional cathode materials. Studies (*He et al., 2022*; *Xie, 2022*) have explored the dual use of magnetite in LIBs, where pure magnetite serves as a cathode, and magnetite coated with conductive or protective layers functions as an anode. These investigations underscore magnetite's potential to enhance battery performance when employed in electrode design. Furthermore, magnetite synthesized through sol-gel techniques has been shown to form a highly porous framework after annealing, facilitating efficient lithium-ion intercalation during the battery discharge process (*Qi et al., 2024*). This porous nature is critical for ensuring a high surface area and effective ionic transport pathways, essential for achieving high capacity and rate performance.

Despite these advantages, pure magnetite faces limitations, such as volume expansion and aggregation during cycling, which can compromise structural integrity and result in capacity fading. Researchers have turned their attention to hybrid structures that integrate magnetite with other materials to overcome these challenges. Hybrid cathodes provide structural stability and exploit the combined phases' synergistic properties to enhance ionic conductivity and lithium-ion storage. Heterogeneous systems that combine nanosized magnetite particles with a second phase capable of lithium intercalation hold immense potential for improving battery performance (*Xie et al., 2024*).

Building on these insights, the present study focuses on synthesizing a hybrid cathode material incorporating magnetite as nanotubes within a sulfur-containing phase. This "colloidal" system aims to achieve a dual benefit – improved ionic conductivity due to the sulfur-containing phase and enhanced lithium storage capacity due to the nanosized magnetite. Additionally, the tubular morphology of magnetite is expected to provide a robust framework that accommodates volume changes during cycling while maintaining structural integrity.

The objectives of this work are twofold: (1) to synthesize and characterize the hybrid cathode material and (2) to investigate the diffusion behavior of lithium ions during the electrochemical intercalation process. By addressing the current challenges associated with pure

magnetite and exploring the potential of hybrid structures, this study aims to contribute to developing next-generation cathode materials for advanced lithium-ion batteries.

Materials and Methods

Following a carefully controlled protocol, a nano-dispersed composite of magnetite and sulfur-containing compounds was synthesized using a hydrothermal method. A 20 mL aqueous ferric sulfate solution ($Fe_2(SO_4)_3$, 0.05 M) was mixed with 5 mL of albumin using magnetic stirring for 5 minutes, yielding a homogeneous orange solution. Subsequently, 8 mL of ethanol (CH_3CH_2OH) was introduced into the solution. To this mixture, 10 mL of 80% hydrazine hydrate ($N_2H_4 \cdot H_2O$) was added dropwise under continuous stirring. After an additional 10 minutes of stirring, the mixture was transferred to a Teflon-lined autoclave and subjected to hydrothermal treatment at 140°C for 24 hours. Upon completion, the autoclave was cooled to room temperature alongside the oven. The inclusion of albumin during synthesis facilitated the formation of magnetite particles with a nanotubular morphology.

The synthesized composite was characterized using X-ray diffraction (XRD), thermogravimetric analysis (TGA), and Mössbauer spectroscopy. XRD patterns were recorded on a DRON-3 diffractometer, while thermal properties were examined using a synchronous thermal analyzer (STA 449 F3 Jupiter). Mössbauer spectra of ^{57}Fe were acquired at 300 K on an MS1104 spectrometer. The isomeric shift values were calibrated relative to α-Fe, employing a 57Co source embedded in a Cr matrix. Spectral analysis and parameter extraction were performed using the Univem MS-2.07 universal software package, ensuring precise decomposition and quantification of spectral components.

The synthesized composite was employed as a cathode material in a custom-designed electrochemical cell featuring a lithium metal anode. The electrolyte utilized was a 1 M solution of lithium tetrafluoroborate ($LiBF_4$) dissolved in γ-butyrolactone (*Nandika et al., 2019*).

Potentiostatic discharge experiments were conducted under a constant current density of j=10 μA to evaluate the cell's performance. Electrochemical impedance spectroscopy (EIS) measurements were performed using an Autolab PGSTAT 12/FRA-2 spectrometer over a frequency range of 0.01 Hz to 100 kHz to assess the system's charge transfer and ionic conductivity. Potentiodynamic studies were performed in the voltage range of 1.0-4.0 V, with voltage sweep rates varying between 0.01 and 0.005 mV/s, to analyze the electrochemical behavior and cycling stability of the cathode material.

This comprehensive suite of electrochemical analyses provided critical insights into the performance characteristics of the synthesized composite as a cathode material in lithium-ion battery systems.

Results and discussion

The first figure (*Figure 1*) presents the results of thermogravimetric analysis (TGA), providing insights into the synthesized composite's thermal stability and decomposition behavior. The initial mass loss of approximately 10 wt.% begins at around 50°C, which can be attributed to the desorption of physically adsorbed water molecules and residual moisture from the powder dried at room temperature. This step is commonly observed in materials with surface-bound water or hygroscopic properties.

A more pronounced mass loss, approximately 33.79 wt.%, is observed within the 200–380°C. This is associated with the thermal decomposition of iron (III) hydroxides $Fe(OH)_3$ into iron oxides (Fe_2O_3) (*Taneja et al., 2023*). This transformation involves the release of water molecules as $Fe(OH)_3$ decomposes into a more thermodynamically stable oxide phase. This process is accompanied by an exothermic peak at ~250°C, indicating the energy release due to the formation of oxide bonds. Such exothermic behavior is characteristic of decomposition reactions leading to stable oxide formations.

In the temperature range of 600–700°C, a further mass loss of ~11.20 wt.% is observed, likely due to the formation of volatile sulfur-containing compounds, such as sulfur trioxide (SO_3). This step suggests the involvement of sulfur in the material's thermal decomposition pathway, possibly arising from the sulfur-containing phase integrated during synthesis. The release of SO_3 may indicate the partial decomposition or volatilization of sulfur-containing moieties within the composite.

Notably, no distinct exothermic peaks are observed beyond 700°C, suggesting that the synthesized compound does not undergo first-order phase transitions in this temperature range. This thermal behavior implies that the material's crystalline framework remains stable at elevated temperatures, which is advantageous for its potential applications in environments requiring high thermal stability.

X-ray diffraction (XRD) analysis, as illustrated in the appendix (*Figure 2*), indicates that the synthesized powder is X-ray amorphous. This conclusion is based on the absence of sharp, well-defined diffraction peaks in the pattern, typically indicative of a crystalline structure with long-range periodic atomic arrangement. Instead, the XRD profile exhibits a broad diffuse halo, which is characteristic of materials with a disordered or amorphous atomic structure.

The Mössbauer spectra of the synthesized material, presented in the appendix (*Figure 3*), reveal the absence of a magnetically ordered state for iron, as evidenced by the lack of hyperfine splitting typically observed in ferromagnetic or antiferromagnetic phases. Instead, the spectra display a series of paramagnetic doublets indicative of iron in a paramagnetic state. This behavior is consistent with a disordered structure where iron cations are not magnetically coupled, likely due to the fine dispersion of the material.

Among the observed doublets, the parameters of Doublet_2 (*Table 1*) are particularly noteworthy. Its high isomer shift (I_S = 1.6075 mm/s) and quadrupole splitting (Q_S = 2.5739 mm/s) suggest that Fe^{3+} cations are in a symmetric oxygen coordination environment. This symmetric environment implies that the iron centers are stabilized within a chemically homogeneous matrix, which aligns with the amorphous nature of the material as identified by X-ray diffraction analysis.

The doublets' relative area percentages (S%) and line widths (G) provide further insight into the material's structural characteristics. Doublet_1, representing most of the spectral contribution (S=57.45%), corresponds to Fe^{3+} in a less distorted environment. At the same time, the remaining doublets (Doublets 2–5) reflect iron cations in environments with varying degrees of asymmetry and electronic interactions. This distinct quadrupole splitting across the doublets suggests the presence of multiple iron sites with diverse local geometries, indicative of a non-crystalline, heterogeneous matrix.

The absence of a magnetically ordered component corroborates the X-ray diffraction results, which identified the material as X-ray amorphous. This lack of magnetic ordering underscores the nanoscale dispersion of the iron-containing phases, as the spatial separation and structural disorder prevent the establishment of magnetic interactions necessary for long-range ordering.

The SEM images presented in the appendix (*Figure 4*) reveal that the synthesized material consists of magnetite nanotubes embedded within agglomerated complexes. These complexes form compact globular structures characterized by a relatively uniform distribution of Fe_3O_4 throughout the volume. The observed morphology suggests effective integration of the magnetite phase within the colloidal system, contributing to the material's overall structural homogeneity.

The X-ray diffraction data further supports the presence of a complex colloidal structure, which confirms the material's X-ray amorphous nature. The lack of distinct crystalline features in the diffractogram aligns with the disordered arrangement of the magnetite nanotubes and their incorporation into the agglomerates, emphasizing the nanoscale dispersion and amorphous characteristics of the synthesized compound.

The figure (*Figure 5*) displays the discharge curves of the first three cycles for an electrochemical cell employing the synthesized material as the cathode. The discharge profiles exhibit a relatively stable operating voltage of approximately 2.2 V throughout the cycles. This voltage is acceptable for developing a 2-volt energy storage device, demonstrating the material's potential for practical applications.

The stability of the operating voltage during discharge indicates consistent electrochemical behavior (*Table 2*) and suggests a reversible lithium-ion intercalation process within the cathode material (*Taneja et al., 2023*). The observed voltage plateau is likely associated with redox reactions involving Fe^{3+}/Fe^{2+} transitions, characteristic of magnetite-based systems. Such stable discharge characteristics are critical for maintaining energy density and ensuring reliable performance in applications requiring low-voltage sources.

The absence of significant voltage fluctuations over the three cycles implies good cycling stability and efficient charge transfer kinetics at the electrode-electrolyte interface. This behavior suggests that the synthesized material exhibits low polarization and retains its structural integrity during repeated lithium-ion insertion and extraction (*Wang et al., 2016*), which are essential properties for long-term operational stability.

The discharge curves and associated parameters demonstrate that the synthesized cathode material combines high specific capacity and energy density with good cycling stability. The initial variations in performance metrics are consistent with typical behavior observed in newly developed materials and could be mitigated by optimizing the synthesis process or material composition. These results position the synthesized material as a strong candidate for cathode applications in lithium-ion batteries, with further investigations into long-term cycling performance and impedance characteristics recommended to understand and enhance its capabilities thoroughly.

The results of the discharge cycles indicate that the synthesized material exhibits promising electrochemical performance, with specific capacity, specific energy, stoichiometric factor, and efficiency showing consistent trends across the first three cycles. The specific capacity C is

365.1 A·h/kg in the first cycle, which decreases slightly to 345.1 A·h/kg in the second cycle before recovering to 363.5 A·h/kg in the third cycle. This initial drop is likely due to stabilization processes within the material, such as structural rearrangement or forming a solid electrolyte interphase (SEI) layer. The recovery in the third cycle demonstrates that the material retains its capacity for reversible lithium-ion intercalation, suggesting good cycling stability.

Similarly, the specific energy E follows a comparable pattern, starting at 790.2 W·h/kg in the first cycle, decreasing to 697.1 W·h/kg in the second, and stabilizing at 695.4 W·h/kg in the third cycle. This decrease aligns with the slight reduction in specific capacity and may result from minor irreversibility in lithium-ion intercalation and deintercalation or resistive losses at the electrode-electrolyte interface. Despite this, the values indicate that the material is capable of providing significant energy density, which is critical for practical applications.

The stoichiometric factor x, which reflects the extent of lithium-ion intercalation, remains relatively stable across the cycles, with values of 2.7, 2.6, and 2.8. These results indicate the efficient utilization of lithium ions, further supported by the material's ability to maintain its structural integrity throughout the cycles. The efficiency η is initially high at 96% but drops to 83% in the second cycle before partially recovering to 85% in the third cycle. The initial drop in efficiency may be attributed to resistive losses or side reactions, such as electrolyte decomposition or partial capacity fading due to structural changes in the cathode material. The slight recovery in the third cycle suggests that these processes stabilize, highlighting the material's durability.

To evaluate the kinetics and extent of lithium-ion intercalation within the synthesized cathode material, the lithium diffusion coefficient D_{Li} was determined using potentiodynamic curves (*Figure 6*). These curves were recorded at varying scan rates, ranging from 0.01 to 0.005 mV/s. The discharge region of the curves exhibits a distinct cathodic peak, characteristic of the electrochemical reduction process associated with lithium-ion intercalation into the host material.

As the scan rate increases, notable changes in the peak behavior are observed. Specifically, the cathodic peak becomes less pronounced and shifts to lower voltages. This behavior indicates kinetic limitations during faster scanning, reducing the time lithium ions can diffuse into the active material. The peak shift also suggests an increase in overpotential at higher scan rates, likely due to the effects of slower charge transfer kinetics and the diffusion limitations of lithium ions within the material.

The cathodic peak current and scan rate relationship provide additional insight into the intercalation mechanism. As shown in the appendix (*Figure 7*), the cathodic current at the peak value varies systematically with the scan rate, reflecting the influence of diffusion processes on electrochemical performance. By analyzing this dependence, the lithium diffusion coefficient can be extracted using the Randles-Sevcik equation (*Huang et al., 2012*) for semi-infinite linear diffusion.

The equation (*Huang et al., 2012*),

$$i_p = \left(2.69\times10^5\right) n^{3/2} A D_{Li}^{1/2} C \upsilon^{1/2}$$

relates the peak current i_p to the scan rate ν, diffusion coefficient D_{Li}, active electrode surface area A, and the lithium-ion concentration C.

The observed peak shifts and the current's scan rate dependence suggest that lithium-ion diffusion is the rate-limiting step at higher scan rates. This behavior highlights the importance of optimizing the material's structure to enhance ionic conductivity and minimize resistance to lithium transport. The nanoscale and amorphous nature of the synthesized material likely contributes to its overall lithium storage capacity by providing abundant intercalation sites and shorter diffusion pathways. However, further structural refinement and compositional tuning could improve the material's performance under dynamic conditions.

The lithium-ion diffusion coefficient D_{Li} was calculated from potentiodynamic measurements using the Randles-Sevcik equation, which correlates the peak current (i_p) to the electrochemical and physical properties of the electrode material and the experimental conditions (*Prosini, 2002*). The relationship is expressed as:

$$i_p = \frac{n^{\frac{3}{2}} F^{\frac{3}{2}}}{R^{\frac{3}{2}} T^{\frac{1}{2}}} D^{\frac{1}{2}} A_{c_{Dx}} v^{\frac{1}{2}}$$

where i_p is the peak current obtained from the cyclic voltammogram, R is the universal gas constant (8.314 J mol−1 K−1), T is the absolute temperature (298 K for room temperature), n is the number of electrons transferred during the electrochemical reaction (for lithium-ion intercalation, n=1), A is the contact area between the cathode and the electrolyte (approximated as the geometric area of the electrode), C is the concentration of lithium ions within the cathode (0.024 mol cm−3), calculated from the unit cell volume of the active material), and v is the potential scan rate.

In the context of the cathodic process, the initial concentration of vacancies in the intercalation host c_0 serves as the critical parameter, while for the anodic process, c_0 corresponds to the initial concentration of lithium ions within the intercalation matrix. Assuming that the intercalation and deintercalation processes are reversible under standard conditions, the lithium diffusion coefficient D_{Li} at room temperature (T = 298K) was calculated as

$$i_p = (2.69 \cdot 10^5) n^{\frac{3}{2}} A D_{Li^+}^{\frac{1}{2}} c_{Li} v^{\frac{1}{2}}, \text{ D = 1.4 } 10^{-13}, \text{ cm}^2/\text{s}.$$

To further validate and refine this value, the lithium diffusion coefficient was independently determined using the method of electrochemical impedance spectroscopy (EIS) (*Han et al., 2024*). EIS is a powerful tool that measures the frequency-dependent impedance of an electrochemical cell, providing insights into the kinetic and transport processes governing the system. The analysis is based on the construction of Nyquist plots (impedance hodographs) and their subsequent interpretation through equivalent circuit modeling.

The method incorporates the Warburg impedance, which is sensitive to the diffusion of lithium ions in the electrode (*Cruz-Manzo & Greenwood, 2020*). In the low-frequency region of the Nyquist plot, the Warburg impedance appears as a linear segment with a slope of 45°, representing the diffusive contribution. The Warburg constant W is extracted from the impedance data and is related to the lithium diffusion coefficient D_{Li} by the following relationship:

$$D_{Li} = \frac{R^2 T^2}{2 A^2 n^4 F^4 C_0^2 W^2}$$

where R is the universal gas constant 8.314 J mol−1 K−1), T is the absolute temperature, A is the active electrode surface area, n is the number of electrons transferred during the reaction, F is the Faraday constant (96,485 C mol-1), C_0 is the bulk lithium-ion concentration in the electrode, and W is the Warburg constant.

The Warburg constant W is determined by fitting the linear portion of the low-frequency region of the Nyquist plot.

$$-\operatorname{Im} Z = \frac{W}{\sqrt{4\pi f}}$$

The slope of this segment reflects the contribution of diffusion-controlled processes, allowing the calculation of D_{Li}. This method's accuracy relies on proper circuit modeling and precise measurement of impedance across a broad frequency range.

The Warburg constant, in turn, is related to the dependence of the equilibrium potential on the concentration of the diffusing element c:

$$W = \frac{-dE/dc}{F\sqrt{D}}$$

D is the diffusion coefficient of lithium in the cathode.

The relationship between E and c is determined from the quasi-equilibrium discharge curve (dependence on the amount of transferred charge Q):

$$dQ = \frac{dcnF}{\rho}$$

Where ϱ is the density of the cathode material.

So, based on the equations, we can obtain an expression for the diffusion coefficient D:

$$D = \frac{\left(dE/dQ\right)^2}{2\rho^2 W^2} = \frac{\left(dE/dQ\right)^2}{4\pi f \rho^2 \left(\operatorname{Im}\right)^2}$$

The diffusion coefficient value calculated by the electrode impedance spectroscopy method for three discharge cycles is

$D \approx 3.0 \cdot 10^{-13} - 8.9 \cdot 10^{-13}$ cm^2/s.

The D values obtained based on independent methods coincide with an accuracy of an order of magnitude, which is evidence of the correctness of the obtained results.

Conclusions

This study demonstrates the successful synthesis and electrochemical characterization of a mesoscopic compound featuring nano-dispersed magnetite as the active cathode material for lithium-ion batteries. The cathode exhibited a flat discharge curve with a stable operating voltage of approximately 2.2 V, making it suitable for low-voltage energy storage systems. Its specific electrochemical capacity, measured at ~350 A·h/kg, remained consistent over the three discharge cycles investigated, highlighting the material's excellent cycling stability and structural integrity.

The lithium-ion diffusion coefficient, determined through potentiodynamic measurements and impedance spectroscopy, ranged between (3.0 10^{-13}) and (8.9 10^{-13}) cm^2/s. These values are notably high for systems of this type, indicating efficient ionic transport within the material. The

nanoscale dispersion of magnetite and the amorphous nature of the synthesized compound likely contribute to its superior diffusion kinetics and reversibility during lithium intercalation and deintercalation.

The material's performance, including its stable discharge behavior, high-capacity retention, and favorable diffusion properties, positions it as a promising candidate for cyclic operation in lithium current sources. These results suggest that further optimization of the synthesis process and structural properties could unlock additional improvements, enhancing the material's suitability for advanced energy storage applications.

References:

Adi, A., & Taniguchi, I. (2022). Synthesis and characterization of porous-crystalline C/Fe_3O_4 microspheres by spray pyrolysis with steam oxidation as anode materials for Li-ion batteries. *Advanced Powder Technology: The International Journal of the Society of Powder Technology*, *33*(6), 103606. https://doi.org/10.1016/j.apt.2022.103606

Cruz-Manzo, S., & Greenwood, P. (2020). An impedance model based on a transmission line circuit and a frequency dispersion Warburg component for the study of EIS in Li-ion batteries. *Journal of Electroanalytical Chemistry*, *871*(114305), 114305. Lausanne, Switzerland. https://doi.org/10.1016/j.jelechem.2020.114305

Ding, L., Dong, Y., Lu, Q., Zhou, H., Fan, Q., Kuang, Q., & Zhao, Y. (2024). Nickel pre-intercalated bilayer vanadium pentoxide hydrate for reversible structural evolution in Na-ion battery cathode. *Journal of Alloys and Compounds*, *970*(172729), 172729. https://doi.org/10.1016/j.jallcom.2023.172729

Han, G., Hu, Q., Gao, K., & Yao, J. (2024). Boosting the intrinsic kinetics of lithium vanadium phosphate via an electrochemically active cross-link framework. *Journal of Alloys and Compounds*, *1007*(176516), 176516. https://doi.org/10.1016/j.jallcom.2024.176516

He, X., He, Y., Wang, C., Zhu, B., Liu, A., & Tang, H. (2022). Oxygen vacancy-rich Fe3O4 nanoparticle synthesized via facile electrochemical method as anode material for high-performance lithium-ion batteries. *The Journal of Physics and Chemistry of Solids*, *171*(111028), 111028. https://doi.org/10.1016/j.jpcs.2022.111028

Heydari Gharahcheshmeh, M., & Chowdhury, K. (2024). Fabrication methods, pseudocapacitance characteristics, and integration of conjugated conducting polymers in electrochemical energy storage devices. *Energy Advances*, *3*(11), 2668-2703. https://doi.org/10.1039/d4ya00504j

Hou, W., Wang, Q., Li, Z., Lyu, N., Zhong, W., Jin, Y., Liang, T., & Wei, R. (2025). Hydrogen sensors of Ce-doped MoS_2 with anti- humidity for early warning thermal runaway in lithium-ion batteries. *Sensors and Actuators. B, Chemical*, *425*(136988), 136988. https://doi.org/10.1016/j.snb.2024.136988

Huang, Y.-H., Wang, F.-M., Huang, T.-T., Chen, J.-M., Hwang, B.-J., & Rick, J. (2012). Micro-electrode linked cyclic voltammetry study reveals ultra-fast discharge and high ionic transfer behavior of $LiFePO_4$. *International Journal of Electrochemical Science*, *7*(2), 1205-1213. https://doi.org/10.1016/s1452-3981(23)13408-0

Jonak, S., & Borah, J. P. (2021). Correlation between cation distribution and heating efficiency of annealed Fe_3O_4 nanoparticles. *Materials Today. Communications*, *26*(101789), 101789. https://doi.org/10.1016/j.mtcomm.2020.101789

Li, S., Liu, H., Kong, F., Lu, C., Chen, J., Tao, S., & Qian, B. (2024). In-situ synthesis of Fe_3O_4@Fe_3C nanoparticles with heterostructures embedded in the N-doped porous carbon for high-performance lithium-ion batteries. *Journal of Energy Storage*, *97*(112967), 112967. https://doi.org/10.1016/j.est.2024.112967

Mendonça, J. P., Lima, S. L., Romano, P. N., de Almeida, J. M. A. R., Santos, S. F., Liu, L., de Lima, R. B., & Garcia, M. A. S. (2025). Unveiling the Mn^{3+}/ Mn^{4+} and Ni^{2+} potential as a high-capacity material for next-generation energy storage devices. *Catalysis Today*, *445*(115046), 115046. https://doi.org/10.1016/j.cattod.2024.115046

Nandika, A. O., Rochliadi, A., & Patah, A. (2019). Ionic liquids (ILs)-based electrolytes system for lithium-ion batteries. *IOP Conference Series: Materials Science and Engineering*, *622*, 012025. https://doi.org/10.1088/1757-899X/622/1/012025

Prosini, P. (2002). Determination of the chemical diffusion coefficient of lithium in $LiFePO_4$. *Solid State Ionics*, *148*(1-2), 45-51. https://doi.org/10.1016/s0167-2738(02)00134-0

Qi, X., Liu, M., Zhu, W., Wei, Z., Liang, Y., Sun, C., Bao, C., & Zhao, W. (2024). Spherical Fe_3O_4 morphology modulation for enhancing infrared emissivity and radiant heat dissipation. *Optical Materials*, *152*(115541), 115541. https://doi.org/10.1016/j.optmat.2024.115541

Su, H., Song, Z., Liu, Z., Li, H., Xu, M., & Wang, G. (2024). Optimization of novel power supply topology with hybrid and multielement energy storage for controllable nuclear fusion devices superconducting magnets. *Journal of Energy Storage*, *100*(113603), 113603. https://doi.org/10.1016/j.est.2024.113603

Taneja, L., Kochar, C., Yadav, P. K., Yadav, M., & Tripathy, S. S. (2023). Enhancement of surface area of iron oxide modified by natural moieties towards defluoridation from water and antibacterial properties. *Groundwater for Sustainable Development*, *22*(100954), 100954. https://doi.org/10.1016/j.gsd.2023.100954

Wang, F., Wu, X., Li, C., Zhu, Y., Fu, L., Wu, Y., & Liu, X. (2016). Nanostructured positive electrode materials for post-lithium-ion batteries. *Energy & Environmental Science*, *9*(12), 3570-3611. https://doi.org/10.1039/c6ee02070d

Xie, J., Yin, J., Xu, L., & Ahmed, A. (2024). Nanostructured anode materials for high-performance lithium-ion batteries. *Journal of Alloys and Compounds*, *1008*(176620), 176620. https://doi.org/10.1016/j.jallcom.2024.176620

Xie, Y., Qiu, Y., Tian, L., Liu, T., & Su, X. (2022). Ultrafine hollow Fe3O4 anode material modified with reduced graphene oxides for high-power lithium-ion batteries. *Journal of Alloys and Compounds*, *894*(162384), 162384. https://doi.org/10.1016/j.jallcom.2021.162384

Yang, X., Li, P., Guo, C., Yang, W., Zhou, N., Huang, X., & Yang, Y. (2024). Research progress on wide-temperature-range liquid electrolytes for lithium-ion batteries. *Journal of Power Sources*, *624*(235563), 235563. https://doi.org/10.1016/j.jpowsour.2024.235563

Zeng, G., Lin, J., Li, R., & Chen, X. (2025). Investigation on novel two-dimensional BC2P monolayer: A promising anode with high theoretical capacity for Na-/Li-ion batteries. *Journal of Power Sources*, *625*(235638), 235638. https://doi.org/10.1016/j.jpowsour.2024.235638

Appendix

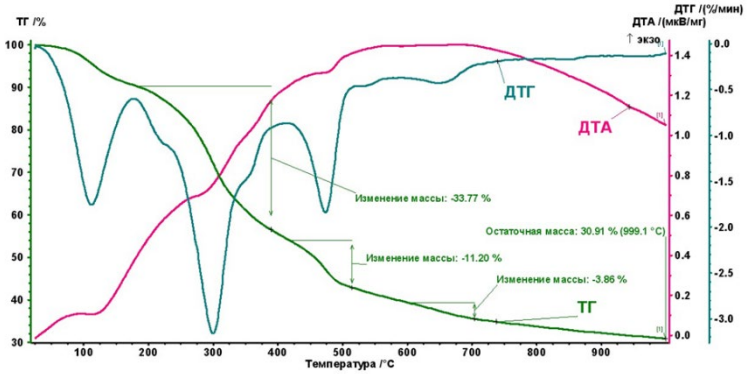

Figure 1. Thermogravimetric analysis of the composite, showing mass losses from water desorption (~50°C), iron (III) hydroxide decomposition (200-380°C), and volatile sulfur compound formation (600–700°C), with an exothermic peak at ~250°C indicating oxide formation.

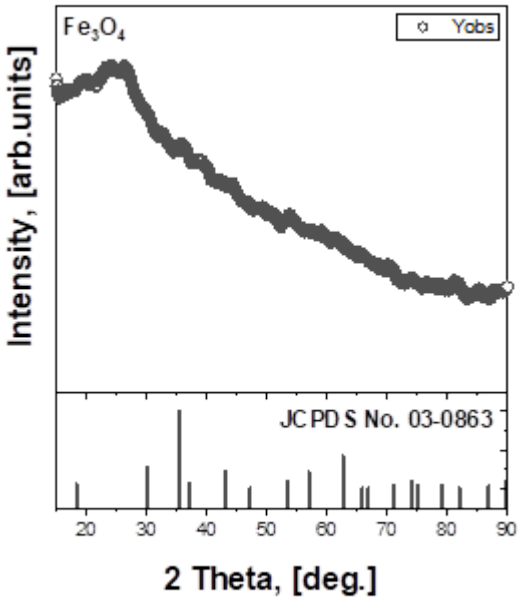

Figure 2. X-ray diffraction pattern of the synthesized material, exhibiting a broad diffuse halo characteristic of an X-ray amorphous structure, indicative of a disordered atomic arrangement and the absence of long-range crystallinity

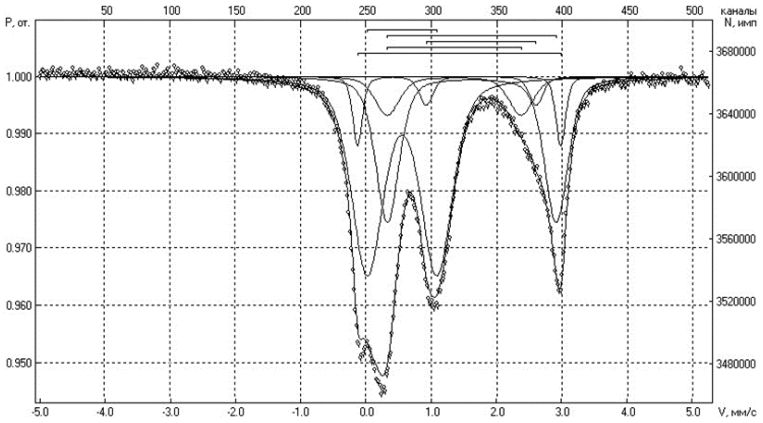

Figure 3. Mössbauer spectrum of 57Fe at room temperature, showing paramagnetic doublets indicative of Fe3+ cations in a disordered environment, with no evidence of magnetically ordered states

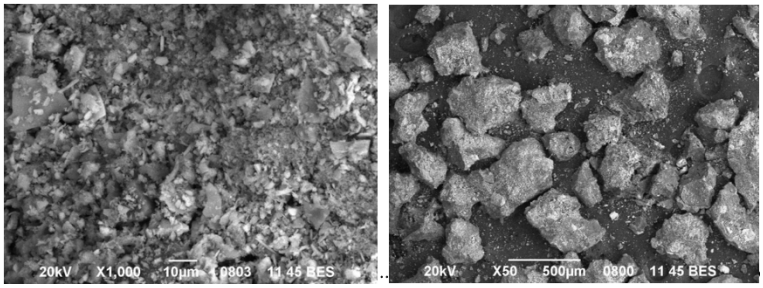

Figure 4. SEM images of the synthesized material, highlighting the structural features and morphology

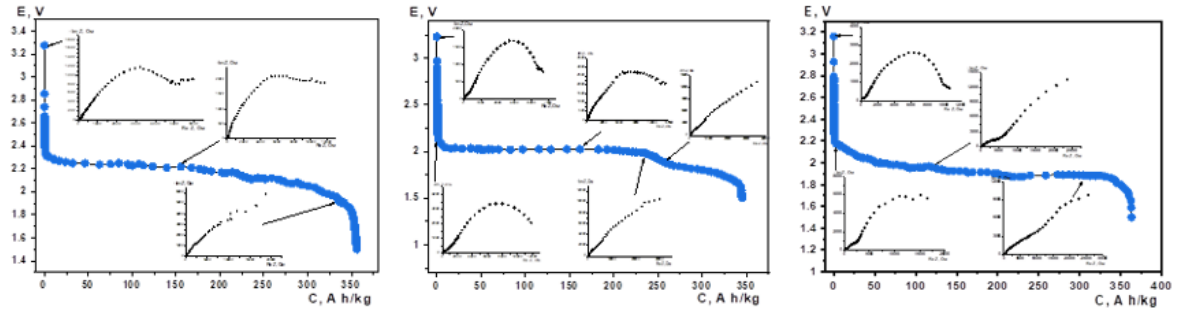

Figure 5. Discharge curves for the 1st, 2nd, and 3rd cycles of the electrochemical cell, accompanied by the corresponding impedance spectra

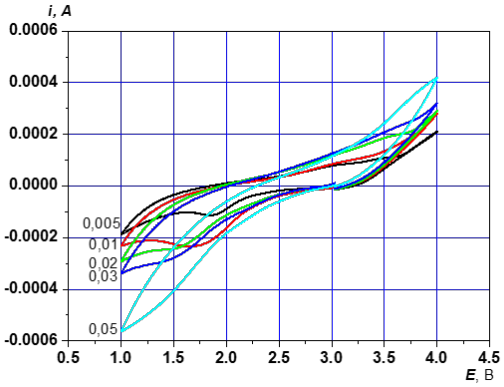

Figure 6. Cyclic voltammetry curves of the composite electrode, recorded at various potential sweep rates at 25°C, illustrating the electrode material's electrochemical behavior and kinetic responses

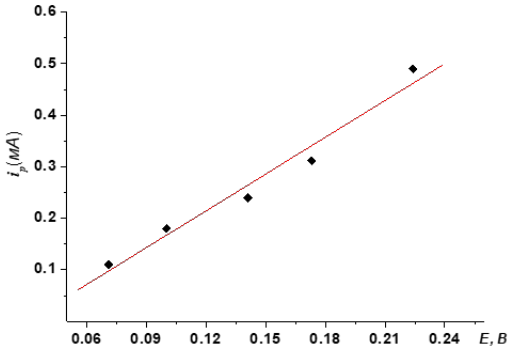

Figure 7. Dependence of the cathodic peak current on the square root of the potential sweep rate from cyclic voltammetry measurements. The solid line represents the linear fit to the experimental data, indicating a diffusion-controlled process

Table 1. Parameters of RT Mössbauer spectra of ^{57}Fe

Component	IS, mm/s	QS, mm/s	S, %	G, mm/s
Doublet_1	0.5839	0.9946	57.45	0.6491
Doublet_2	1.6075	2.5739	24.58	0.3754
Doublet_3	1.7115	1.6035	2.31	0.2203
Doublet_4	1.3819	1.9649	7.08	0.4241
Doublet_5	1.4313	3.1012	8.57	0.2160

Table 2. Electrochemical discharge characteristics of the synthesized material

No. of discharge cycle	Specific Capacity, C, A·h/kg	Specific Energy, E, W·h/kg	Stoichiometric Factor, x	Efficiency, η
1	365.1	790.2	2.7	96
2	345.1	697.1	2.6	83
3	363.5	695.4	2.8	85